Pore-scale kinetics of calcium dissolution and secondary precipitation during geological carbon storage

Na Liu [a,*], Malin Haugen [a], Benyamine Benali [a], David Landa-Marbán [b], Martin A. Fernø [a,b]

[a] *Department of Physics and Technology, University of Bergen, Allégaten 55, 5007 Bergen, Norway*
[b] *Energy & Technology, NORCE Norwegian Research Centre AS, Nygårdsgaten 112, 5008 Bergen, Norway*

ARTICLE INFO

ABSTRACT

Geological carbon storage (GCS) in deep underground formations presents a significant opportunity to mitigate anthropogenic emissions of carbon dioxide in the context of climate change. The injected carbon dioxide may acidify the formation brine and dissolve carbonate minerals in the storage formations. Understanding the dynamics of carbonate dissolution at reservoir conditions is crucial for assessing the integrity and stability of reservoir rocks. Using carbonate-functionalized micromodels we investigate the pore-scale dynamics of carbonate dissolution and shed light on the interplay between surface reactions and mass transfer with relevance for geological carbon storage. Our experimental observations reveal the complex interplay between carbon dioxide exsolution/mineralization and mineral dissolution/precipitation during injection. Local chemical reactions and hydrodynamics impact the dissolution rate, whereas the presence of a free carbon dioxide phase can impede carbonate dissolution. Hence, we provide new experimental data that enhance our fundamental understanding of coupled geochemical GCS reactions that can augment the development of accurate and reliable constitutive models that assess leakage risks and the stability of mitigation techniques such as microbial-induced carbonate precipitation.

1. Introduction

Geological carbon storage (GCS) may mitigate anthropogenic carbon dioxide (CO_2) emissions and contribute to achieve Net-Zero Carbon emissions by 2050 (Pachauri and Reisinger, 2007). Captured carbon dioxide is injected into deep subsurface geological storage sites, such as saline aquifers and depleted hydrocarbon reservoirs, where the CO_2 is permanently stored through a range of trapping mechanisms acting at different length and time scales. Dissolution trapping occurs when the injected CO_2 partly dissolves into the aqueous phase, and the dissolution rate is influenced by the reservoir temperature, pressure and brine salinity (Chang et al., 2017). The aqueous phase acidity increases during the dissolution process (Morais et al., 2016), and the purity of the injected CO_2 stream determines the pH of carbonated formation brine, which can reach highly acidic levels as low as 1 in the presence of NO_2 and SO_2 (Ellis et al., 2010). Consequently, geochemical interactions occur between the acidic aqueous phase and carbonate minerals within the storage formation, potentially inducing mineral dissolution that could affect CO_2 plume migration and increase the risk of leakage (Deng et al., 2013; Deng et al., 2015).

To mitigate such risks, microbial-induced calcium carbonate precipitation (MICP) has been suggested as a mitigating technology that forms hydraulic barriers in pre-existing or new CO_2 leakage pathways (Cunningham et al., 2014; Phillips et al., 2013). However, the introduction of CO_2 into the system could significantly lead to the abrasion of calcite crystals (Mitchell et al., 2013). To estimate the MICP sealing integrity, kinetic studies of carbonate mineral dissolution at reservoir conditions are essential (Mitchell et al., 2013). Moreover, these studies should be performed at timescales where the CO_2 is mobile (Cunningham et al., 2011). Numerous studies have been performed to understand $CaCO_3$ dissolution rates pertaining to CO_2 geological storage under various conditions of temperature, pressure, pH and salinity (Kaufmann and Dreybrodt, 2007; Liu and Dreybrod, 1997; Morse, 2018; Yoon et al., 2019). The intricate mass transfer dynamics within porous media play a pivotal role in influencing the thickness of the diffusion boundary layer at the liquid-solid interface (Liu and Dreybrod, 1997). Notably, during instances of low injection velocities, the weak shear forces from the flow result in diminished acid mass transfer at the interface. This, in turn, leads to mass transfer regimes taking precedence over the dissolution process due to lower mass transfer rates compared to reaction rates.

---

* Corresponding author.
E-mail address: Na.Liu@uib.no (N. Liu).

Furthermore, the wettability of $CaCO_3$ determines the thickness of the water film present on the solid surface, and the dissolution rates have been validated to be linearly dependent on this thickness (Buhmann and Dreybrodt, 1985). Consequently, the kinetics of $CaCO_3$ dissolution in porous media was governed by a plethora of parameters including pH, porous media characteristics, flow velocity, and the intrinsic properties of $CaCO_3$ precipitates (Molins et al., 2014).

However, the underpinning physics and geochemical interactions that form the basis for current understanding of the interplay between pH, flow velocity, and porous media have not been sufficiently validated against experimental data. Micromodels are commonly employed to acquire fundamental insights into physical behaviors, thereby facilitating the development of more precise and robust upscaled constitutive models designed for the continuum scale (Morse et al., 2007). However, conventional micromodels fashioned from materials like glass, silicon, or polymeric, often lack the capacity to faithfully represent real rock mineralogy, and thus are limited in their description of reactive transport (Yoon et al., 2019; Yoon et al., 2012). The functionalization of micromodels for desired chemical and surface characteristics has emerged as an appealing avenue for investigating reactive transport and interfacial phenomena using microfluidics (Haugen et al., 2023b; Xu and Balhoff, 2022).

Within this investigation, we employed carbonate-functionalized micromodels wherein in situ $CaCO_3$ precipitates were generated through the utilization of MICP technology (Liu et al., 2023). This approach allowed us to scrutinize the intricate mechanisms of $CaCO_3$ dissolution within porous media, accentuating the interplay between surface reactions and mass transfer. Our study aims to bridge the gap between simulation and experiment, enabling a more accurate understanding of the complex processes involved in carbonate dissolution within the GCS context. We focus our analysis at the pore-scale, and highlight the importance of local hydrodynamics on reactive transport. New experimental data was provided that shed light on the coupled kinetics of carbonate precipitation and dissolution during CO_2 injection. Our mechanistic approach enables validation and development of more precise and robust constitutive models for the continuum scale studies of MICP as a GCS leakage mitigation technology.

2. Experimental section

2.1. Fluids

To reduce the $CaCO_3$ reactivity within the water phase before CO_2 injection, a low salinity brine (1.12 mmol/L Ca^{2+}) was used instead of pure water. The concentration of Ca^{2+} was calculated based on the solubility of $CaCO_3$ in pure water at test conditions (100 bar, 35 °C) (Coto et al., 2012). Buffer solutions with equal concentrations of phosphoric, acetic and boric acids (see Table 1) were titrated with sodium hydroxide to adjust the pH between 3.0 and 7.0. Carbonated water (CO_2-saturated water) was made by mixing CO_2 with distilled water at elevated pressure (20 barg above test pressure) and room temperature. The carbonated water was equilibrated using a PEEK accumulator for seven days. The pH of carbonated water was calculated to 3.11 based on the CO_2 solubility in water from an improved model (Duan and Sun, 2003). A 'strong' and a 'weak' acid solution (see Table 1) containing different concentrations of HCl acid were used to evaluate the effect of pH on dissolution rate.

2.2. Micromodel and experimental setup

Pore-scale dissolution and precipitation kinetics were studied using a high-pressure microfluidic device with a realistic pore network based on a thin section from a natural sandstone (Liu et al., 2023). The pore network contains 36 (4 columns × 9 rows) repetitions of a unique pore pattern, with an overall porosity of 0.61 and permeability of 2.97 Darcy. The microfluidics has four injection ports and two distribution channels (connecting port 1 to 2, and port 3 to 4) allowing fluid injection and/or production through the pore network (Fig. 1). Dynamic pore-scale processes were captured with a Zeiss fluorescent microscope (Axio Zoom. V16, Zeiss) with a motorized scanning stage. Pore pressure was controlled by a high precision plunger pump (Quizix Q5000–10 K), and a back pressure regulator (EB1ZF1 Equilibar Zero Flow) connected to a pressurized 1 L nitrogen cylinder at 100 bar. Temperature was kept constant at 35 ± 0.5 °C by circulating warm water through internal copper tubes in the chip holder. A more detailed description of the experimental setup is found elsewhere (Benali et al., 2022; Haugen et al., 2023a).
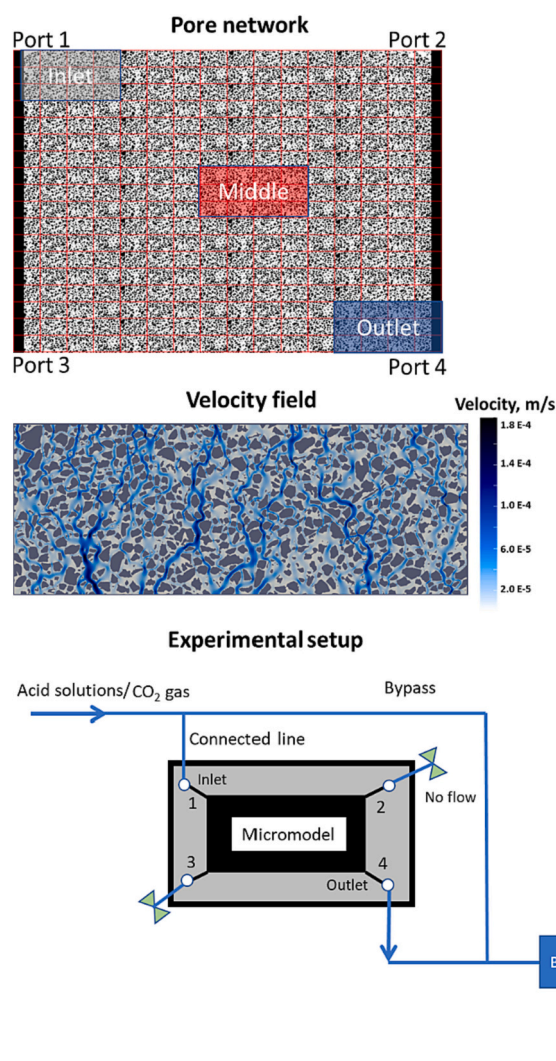
2.3. Fluorescence imaging

The aqueous phase pH changes during $scCO_2$ drainage were visualized and quantified using a fluorescent pH indicator (pHrodo™ Red, ThermoFisher). The fluorescent intensity has an inverse functional relationship with pH; low intensity at alkaline conditions, and increases as the pH decreases (Scientific, 2022). The fluorescence intensity was calibrated to visualize and quantify CO_2 mass transfer at the pore scale (Fig. 2). For calibration, each buffer solution mixing with 8 μmol/L dye was injected into the micromodel at experimental conditions (100 barg and 35 °C) for >50 PVs. Continuous scans were taken for 24 h with intervals of 20 min and the average fluorescent intensity was calculated. During imaging, both light intensity and exposure time were kept constant. The plot of pH and intensity shows the calibration relationship fits the following equation with adjusted r-squared (R^2) of 0.998, consistent with previous measurements (Chang et al., 2016; Chang et al., 2017). Therefore, the pH value of the aqueous phase was quantified from the fluorescence images with a maximum uncertainty of ±0.75. Note that the fluorescence-pH relationship is only calibrated for pH range 3.0 to 7.0, and cannot accurately represent aqueous phase pH outside this range.

$$Fluorescence\ intensity = 624.52 - 268.75pH + 55.06pH^2 - 3.82pH^3 \qquad (1)$$

2.4. Image analysis

Pore network images were captured using a microscope equipped with both brightfield and fluorescence channels. The whole pore network, comprising a total of 121 distinct images, was acquired in 277 s. These images, depicting the pore network in both fluorescence and brightfield channels, were continuously recorded during the injection of CO_2 and acid solutions. For enhanced analysis, translucent crystals were manually assigned a red colour. Extraction of the red-colored crystals was accomplished using a Python script employing the HSV colour thresholder in OpenCV. The size of crystals was calculated by multiplying the number of pixels containing crystals with the pixel area

Table 1
Summary of fluid properties.

Solutions	Composition	Concentration [mM]	pH
Brine	Calcium chloride ($CaCl_2 \cdot H_2O$, 31,306, Sigma-Aldrich)	1.12	6.78
Buffer solutions	Phosphoric, acetic and boric acid (Sigma-Aldrich)	40	3, 4, 5, 6, 7
	Sodium hydroxide (NaOH, > 98% pellets, Sigma-Aldrich)	–	
CO_2-saturated water	Carbon dioxide gas (CO_2, >99.99 mol%)	1340 [a]	3.11
	Distilled water	–	
'Weak' acid	Hydrochloric acid (HCl, ACS reagent, 37%, Sigma-Aldrich)	27.54	1.56
'Strong' acid	Hydrochloric acid (HCl, ACS reagent, 37%, Sigma-Aldrich)	138.04	0.86

[a] calculated based on CO_2 solubility.

Fig. 1. Pore network and experimental setup. <u>Top row:</u> The pore network of micromodel was constructed based on a thin section obtained from an authentic sandstone rock sample. The porous pattern constitutes 36 repetitions (arranged in a 4 × 9 configuration) of a smaller unique pattern, which was split into 16 columns and 18 rows for measurement of local crystal/gas saturation and porosity. The pore network was divided into 288 units (18 rows × 16 columns). Three areas of interest (AOIs) were defined: inlet, middle and outlet. Each AOI contained 12 units (3 rows × 4 columns), with comparable pore structure and porosity (inlet: 0.628; middle: 0.641; outlet: 0.623). <u>Middle row:</u> A simulation was performed to visualize the magnitude of steady-state flow velocity within the small unique pattern, excluding the presence of crystals (confer to https://daavid00.github.io/pymm/examples.html#image for details on the simulation setup). <u>Bottom row:</u> A simplified schematic of the experimental setup illustrates the intended flow into the pore network.

resolution (19.18 μm^2/pixel).

Crystal saturation (S_c) was quantified by dividing the crystal size by the pore space. We assume that crystals occupy the entire pore depth and possess a horizontal area as depicted in the 2D segmented images, causing an overestimation of crystal size. For the fluorescence channel image, a two-class separation was performed using the Multi-Otsu algorithm from the scikit-image library (Van der Walt et al., 2014): the grains/CO_2 phase and the water phase (fluorescent tracer). CO_2 saturation (S_g) was then computed as the ratio of the pore space minus the water phase and crystals to the total pore space.

2.5. Experimental procedure

The experimental procedure consists of the following four main steps:

1. Microbial induced carbonate precipitation (MICP): $CaCO_3$ crystals were formed in the pore network via the uratolytic pathway – *Sporosarcina pasteurii* stains produce urease enzymes for hydrolysis of urea, promoting the chemical precipitation of $CaCO_3$. The experimental procedure is detailed in our previous work (Haugen et al., 2023b; Liu et al., 2023; Song et al., 2018).
2. Enabling flow through the pore network: Subsequent to the MICP process, the microfluidic device was disconnected from the setup and placed in a weak acid to open clogged injection and production ports. The pore network remained undisturbed and partly filled with $CaCO_3$ precipitates from step 1 above. Once reconnected, approximately 10 pore volumes (PVs) of brine were injected from port 1 to 2, and port 3 to 4 to remove residual weak acid and bacterial solutions in the ports, near-port pores and channels.
3. Pressurization: The brine saturated pore network was pressurized to operating pressure (100 barg) with brine injection (50 μL/min) through bypass lines against a back pressure regulator. The pressure was controlled by the back pressure regulator at the outlet.
4. Drainage process: Key parameters for six drainage experiments are summarized below (see Table 2) and may be divided into two categories: dissolution mechanisms (Exp M1) and dissolution kinetics (Exp K1-K4). Carbonate dissolution mechanisms were studied during primary drainage with supercritical CO_2 (scCO_2) over a period of 67 h. Kinetic studies (K1-K4) used CO_2-saturated acid solutions (saturated at 120 barg), and injection was maintained until all the crystals in the pore network were dissolved.

The flow and reaction dynamics in the pore network were visualized by the high-resolution fluorescent microscope system, described below.

3. Results and discussions

3.1. Mechanistic study of carbonate dissolution and precipitation during scCO_2 injection

3.1.1. Dynamic reaction-induced carbonate crystal dissolution in a single pore

Reaction-induced carbonate dissolution was studied in single pore initially filled with brine (Fig. 3). The aqueous phase pH decreased during primary drainage with increasing gas saturation (S_g), and the acidic brine reacted with the carbonate crystal to initiate the dissolution process; the formation of bicarbonate ions (HCO_3^-) increased the local aqueous phase pH and restricted further dissolution. The aqueous phase pH reached its minimum (3.52) after 9 h, coinciding with the maximum (554 μm^2/h) crystal dissolution rate. As the crystal size decreased due to the dissolution process, the pH increased from its minimum and regained initial pH values – with a corresponding reduction in the dissolution rate. The pH of brine was inversely correlated with S_g and increased due to the reaction of carbonate dissolution, which produced HCO_3^- and CO_3^{2-}. The dissolution rate scaled linearly with the aqueous phase pH.

The CO_2 mass transfer was dominated by scCO_2 dissolution in the brine and convection of dissolved CO_2 (dsCO_2) in the pore network (Chang et al., 2016). The scCO_2 dissolution is determined by the CO_2 partial pressure and system temperature (Kordač and Linek, 2008), whereas convection of dsCO_2 was strongly influenced by local hydrodynamics and carbonate dissolution (Dhar et al., 2022). The solubility of scCO_2 in brine was 0.2 M, corresponding to an aqueous phase pH of 3.5 (Duan and Sun, 2003). The interfacial area dominated the propagation of CO_2 in the pore network at early times ($\leq$ 8 h), and the pore network tortuosity (Grogan et al., 1988; Rezk et al., 2022) increased the diffusive
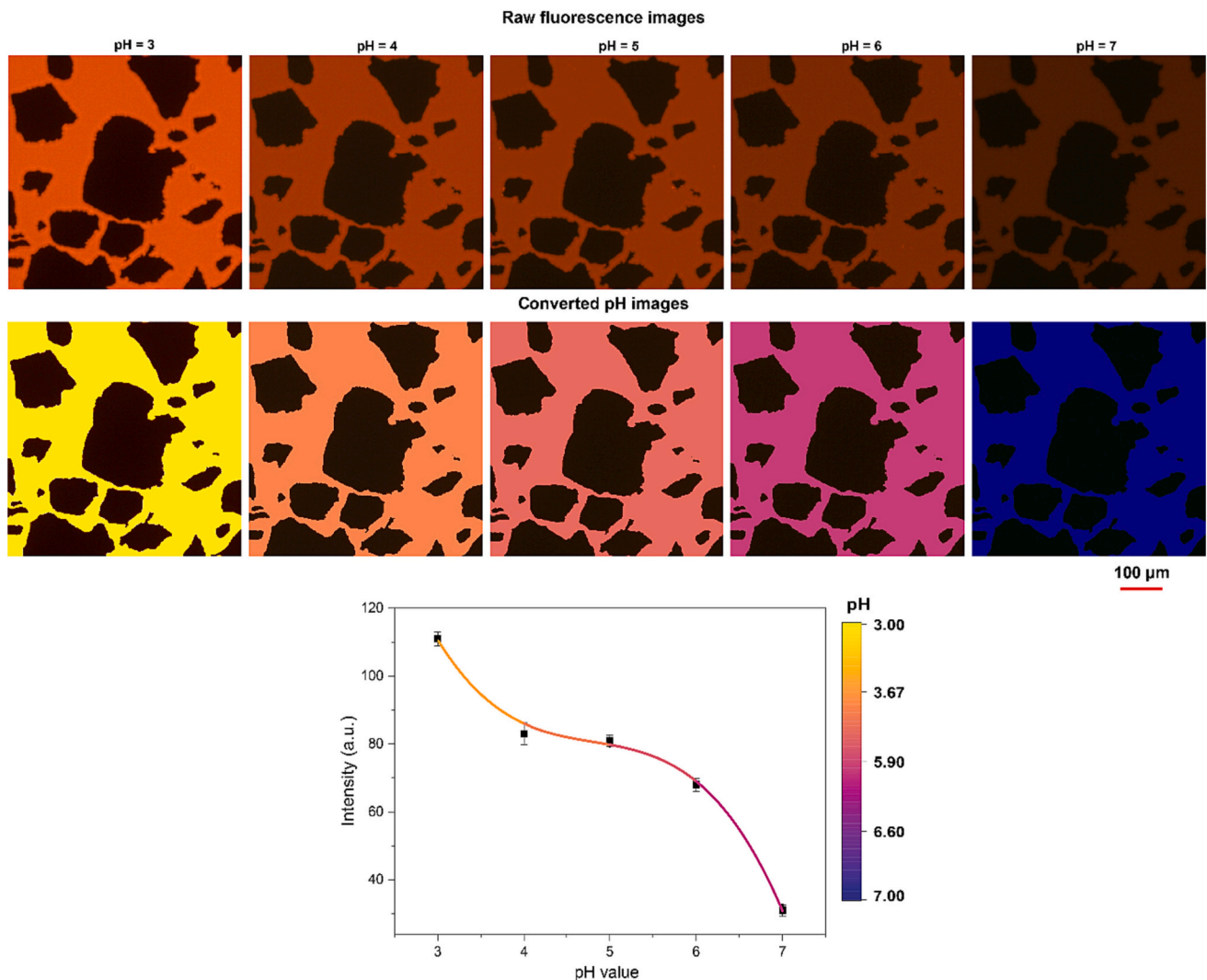
Fig. 2. Calibration between pH and fluorescent intensity for the pHrodo™ Red dye at concentration of 8 μmol/L. Top row: Raw fluorescence images showing the reduction in fluorescence intensity with increasing pH between 3.0 and 7.0. Bottom row: Converted pH images using the pH-fluorescence intensity calibration. Bottom graph: The calibration between fluorescence intensity and pH plotted using the Plasma colormap that scale linearly with fluorescence intensity and pH values calculated from Eq. (1). Error bars represent standard deviations. (For interpretation of the references to colour in this figure legend, the reader is referred to the web version of this article.)

Table 2

Summary of all drainage experiments. All injection test used the same flow velocity (2.03 mm/min), pore pressure (100 barg) and constant temperature (35 °C).

| Exp. #	$S_{crystal, inital}$ [b]	Injection fluid (aqueous phase pH)	Figures
M1[a]	$8.9 \bullet 10^{-2}$	scCO$_2$ (3.50)	Figs. 2-5
K1	$0.93 \bullet 10^{-2}$	CO$_2$-saturated 'strong' acid (0.86)	Figs. 6, 7
K2	$1.6 \bullet 10^{-2}$	scCO$_2$ (3.50) + CO$_2$-saturated 'strong' acid (0.86)	Figs. 6, 7
K3	$1.0 \bullet 10^{-2}$	CO$_2$-saturated 'weak' acid (1.56)	Fig. 6
K4	$1.1 \bullet 10^{-2}$	CO$_2$-saturated deionized water (3.11)	Fig. 8

[a] capillary number [log C$_a$]: −3.65.
[b] initial crystal saturation [fraction of pore volume].

loss; unsaturated CO$_2$-brine was observed in the field of view (FOV). The interfacial area increased with increasing S$_g$, and the minimum aqueous phase pH (pH = 3.52) coincided with the highest dissolution rate (see Fig. 3). The reduction of dsCO$_2$ during carbonate dissolution (because dissolution uses H$^+$ from the reaction dsCO$_2$ + H$_2$O = HCO$_3^-$ + H$^+$) perturbated the solubility equilibrium, enabling further diffusive CO$_2$ mass transfer from the surrounding gas phase into the brine. A temporary reduction of S$_g$ was observed (5.6 percentage points between 10 and 11 h), corroborating that carbonate dissolution increases pH and reduces S$_g$. The changes in brine composition and ionic strength (i.e. increasing Ca^{2+} and HCO$_3^-$ ions) also influenced the CO$_2$ displacement with brine in the pore network (Cao et al., 2015). The flow of CO$_2$ was preferentially through high permeable areas with less flow resistance, consistent with previous work (Kazemifar et al., 2016; Zhang et al., 2011).

Understanding the mechanisms of mineral dissolution-precipitation caused by CO$_2$ injection is of key importance to accurately model fluid flow and forecast GCS security (Lu et al., 2013). The injection of CO$_2$ perturbates the natural geochemical equilibrium by increasing the CO$_2$ partial pressures and reducing the pH of formation water, and thereby initiating the dissolution of carbonate minerals in the near wellbore region. Formation of bicarbonate can also increase the aqueous phase pH downstream to trigger secondary carbonate precipitation (Oelkers et al., 2008). The dissolution and precipitation of minerals influence multiphase flow properties during carbon storage by changing the morphology, porosity, and permeability of the porous rock medium. Our pore-scale observations (Fig. 4) show that the size reduction followed
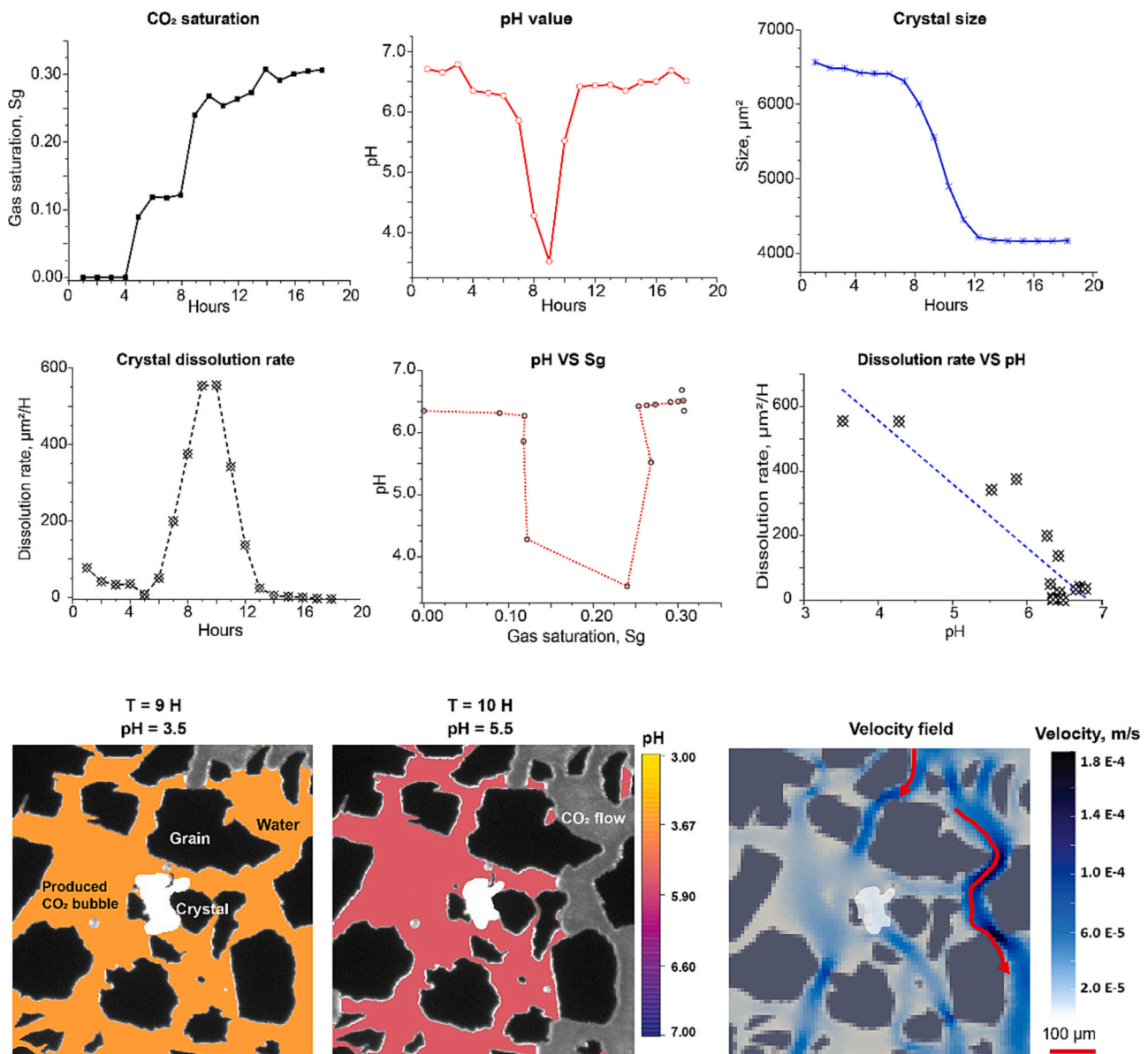
Fig. 3. Dynamic reaction-induced carbonate crystal dissolution in a single pore during primary drainage scCO₂ injection. <u>Top row</u>: Plots of gas saturation (S_g), aqueous phase pH and crystal size. <u>Middle row</u>: Temporal crystal dissolution rate, pH-S_g relationship and the dissolution rate versus aqueous phase pH. $T = 0$ h aligns with initial CO₂ invasion of the entire pore network (not FOV) during primary drainage scCO₂ injection. Each side of the squared FOV is 500 pixels from the crystal center, and the aqueous phase pH was calculated (± 0.03) using the average FOV fluorescence intensity. <u>Bottom row</u>: Visualization of the pore-level gas mass transfer and carbonate dissolution during primary drainage scCO₂ injection using calibrated fluorescence images (aqueous phase pH 3.5 and 5.5). Simulated steady-state FOV flow velocity field (Liu et al., 2023), where the red lines indicate the migration of scCO₂ during drainage coinciding the high velocity regions. (For interpretation of the references to colour in this figure legend, the reader is referred to the web version of this article.)

the aqueous phase pH towards its minimum (3.8) over the first 10 to 15 h. The dissolution reaction consequently buffered the aqueous phase pH, reducing the carbonate dissolution rate and stabilizing the carbonate crystal size after approximately 40 h. Secondary precipitation was then observed (increasing crystal size) until 50 h, coinciding with a reducing of aqueous phase pH (from >6.9 to 6.5) caused by the invasion of scCO₂ in FOV or by increased precipitation of secondary carbonate phases with time.

Carbonate dissolution and precipitation were strongly coupled in the pore, with an inverse relationship between pH and carbonate crystal size; dissolution occurred in a low pH environment, whereas precipitation was associated with an elevated pH. The invasion of scCO₂ triggered secondary carbonate precipitation in the pore, explained by the following aspects: the elevated concentration of dsCO₂ in brine

promoted hydrolysis of H_2CO_3, increasing CO_3^{2-} and H^+ ions in the solution; the dissolution of carbonate increased the concentration of Ca^{2+} and CO_3^{2-} ions in the aqueous phase and increased the pH - which in turn facilitated the $CaCO_3$ precipitation; the solubility of $CaCO_3$ decreased as the salinity and ion strength changed during dissolution, resulting in a high supersaturation; continuous scCO₂ injection induced water evaporation from the brine in the vicinity of the carbonate crystal, leading to salt precipitation (Miri and Hellevang, 2016). Hence, secondary carbonate precipitation was controlled by the local aqueous phase pH, carbonate species concentrations and supersaturation state, consistent with previous work (Hellevang et al., 2019; Lu et al., 2013; Zhu and Lu, 2009).
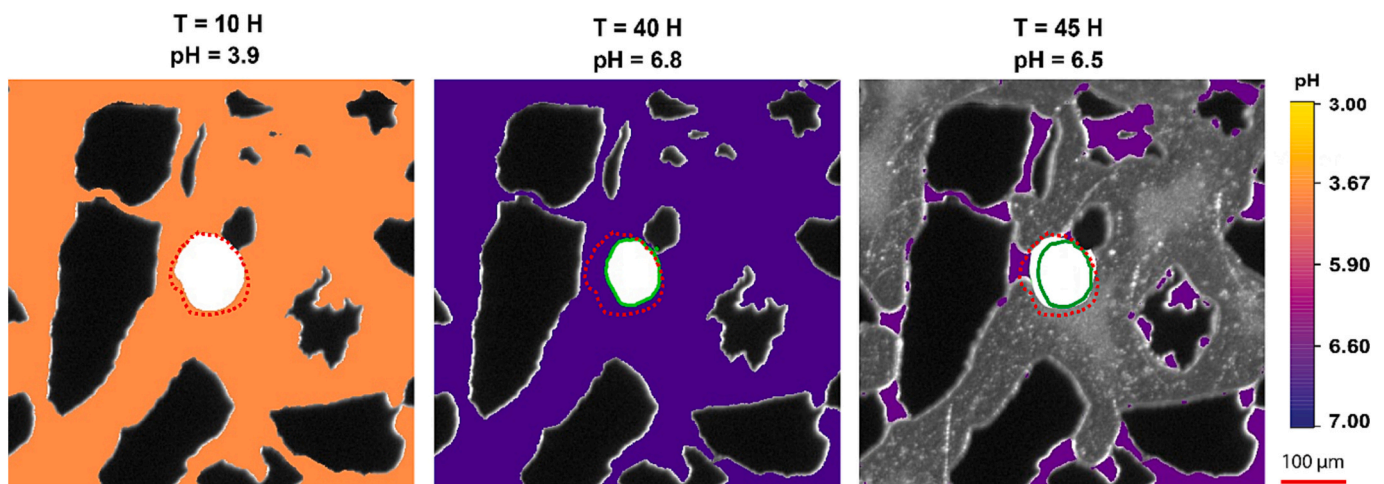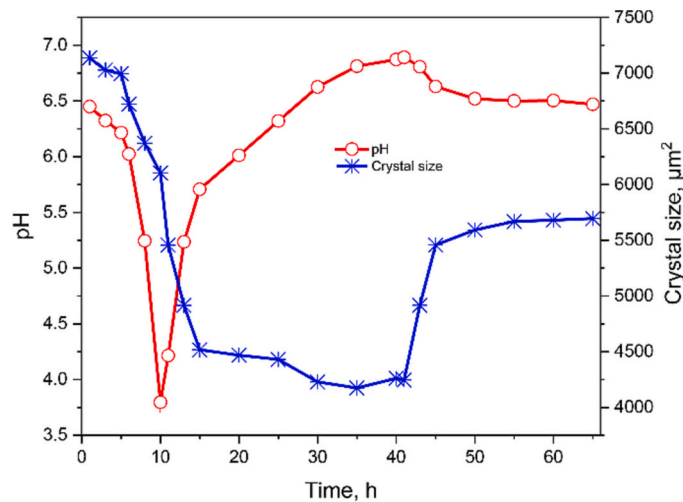
Fig. 4. Carbonate dissolution and secondary precipitation processes during primary drainage scCO$_2$ injection. <u>Top:</u> The relationship between local pH and crystal size. <u>Bottom row:</u> Calibrated fluorescence intensity images show the development in crystal size during the dissolution-precipitation processes for three pH values; at pH 3.9 (after 10 h, initial crystal size indicated with red, dotted line); at pH 6.8 (after 40 h); at pH 6.5 (45 h, crystal size at 40 h indicated with green line). Hence, the size of the carbonate crystal initially decreased (up to 40%) due to dissolution, then increased due to secondary precipitation process as a result of pore-level perturbation of the surrounding aqueous solution that deposited carbonate material onto the crystal surface. <u>Note:</u> From 35 h, the pH measurement was out of calibration range (i.e., pH > 7), underestimating the pH value. (For interpretation of the references to colour in this figure legend, the reader is referred to the web version of this article.)

3.2. The presence of CO$_2$ exsolution and mineralization

The injected CO$_2$ may, under certain conditions, change its state in the subsurface through two main transformation pathways: CO$_2$ exsolution refers to evaporation of gaseous CO$_2$ from a liquid solution, with the associated bubbles or gas pockets forming in a liquid (Al-Amshawee et al., 2021; Allison et al., 2021); whereas CO$_2$ mineralization refers to the process when the CO$_2$ phase converts into stable carbonate compounds (Gadikota, 2021). At the pore-scale (Fig. 5) we observed that both CO$_2$ exclusion and mineralization may co-occur in porous media. Exsolution was observed when the dsCO$_2$ concentration exceeded the CO$_2$ solubility limit, and a free CO$_2$ phase exsolved from the supersaturated aqueous phase. CO$_2$ bubbles nucleated at the carbonate crystal surfaces in regions with low (< 4.0) pH, explained by the following aspects: i. the low pH environment initiated carbonate dissolution and reduced local CO$_2$ solubility; ii. the increased concentrations of HCO$_3^-$ and CO$_3^{2-}$ shifted the equilibrium of H$_2$CO$_3$ hydrolysis via Le Chatelier's principle (Le Chatelier, 1884), leading to supersaturation due to increased dsCO$_2$ at the interface between the crystal and surrounding brine; iii. the rough carbonate crystal surfaces provided ideal nucleation sites for the CO$_2$ exsolution process.

Isolated injected CO$_2$ bubbles were encapsulated with carbonate minerals when they reacted with calcium cations in the water film covering the crystal (Fig. 5). This phenomenon, known as 'CO$_2$ mineral trapping' (Bachu et al., 1994), has significant potential for GCS applications as it can effectively immobilize CO$_2$ for long periods of time. The precipitation process was sustained by upstream carbonate dissolution, creating neutral or even alkaline environments and availability of calcium cations in the solution around the bubble (refer to the images located in the bottom row of Fig. 5).

Overall, these findings provide valuable insights into the mechanisms underlying CO$_2$ mineral trapping and suggest potential pathways for enhancing the effectiveness of geological carbon storage strategies. The CO$_2$ transformation processes occur in the pore during CO$_2$ injection, affecting reservoir properties such as porosity and permeability, and ultimately influencing the transport and mobility of CO$_2$ in the porous media (Xu et al., 2017). The transformation of the injected CO$_2$ in GCS reservoirs could strongly influence the permeability of the rock and fluid paths and a better understanding of transform mechanisms will improve predictions of the long-term CO$_2$ storage safety.
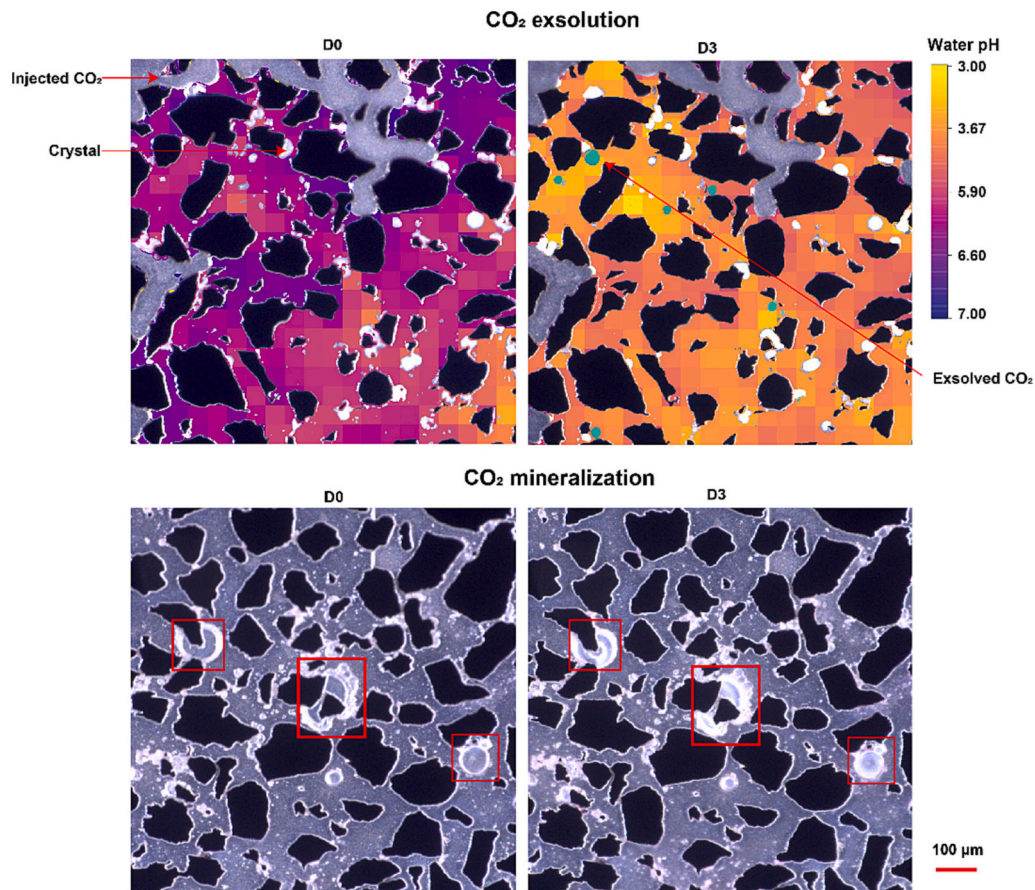
Fig. 5. Transformation of CO_2 in the pore network: CO_2 exsolution and mineralization. <u>Top row</u>: Calibrated fluorescence intensity images (1000 pixels) display the local pH variations during the carbonate dissolution and gas exsolution processes. The initial pH (FOV average pH 6.7) decreased to 3.9 (FOV average) after three days, dissolving the carbonate crystals. During the carbonate dissolution, CO_2 bubbles nucleated and grew on the crystal surfaces. The bubbles preferentially nucleated in regions with low pH. <u>Bottom row</u>: the mineralization process of trapped CO_2 bubbles (red squares). The precipitation of carbonate started at the gas-water interface and grew towards the center of CO_2 bubble to form hollow $CaCO_3$ microspheres. <u>Note</u>: The pH measurement was out of calibration range (i.e., pH > 7) after 10 h and local pH values were therefore not achievable for the mineralization process. (For interpretation of the references to colour in this figure legend, the reader is referred to the web version of this article.)

3.3. Porosity changes by dissolution and secondary precipitation

Geochemical reactions that cause carbonate dissolution/precipitation can occur during CO_2 injection, leading to temporal changes in the pore morphology, local flow velocities and porosity. Carbonate dissolution was initially observed in the entire pore network (Fig. 6) due to low pH of the aqueous phase. Initially, the injection of CO_2 caused a decrease in the pH of the aqueous phase, initiating the dissolution of carbonate crystals. After 10 h of injection, approximately 12.5% of the carbonates underwent dissolution primarily at the inlet, leading to an increase in porosity and S_g. After 40 h, secondary precipitation and CO_2 mineralization enhanced the overall carbonate saturation (S_c). Isolated CO_2 bubbles reacted with calcium cations and formed new minerals, causing a reduction in S_g. The newly formed minerals, however, were susceptible to dissolution or detachment from the pores due to the flow of CO_2. The carbonate dissolution increased local porosity (and permeability), enhancing CO_2 mobility during injection and accelerating further geochemical reactions. The dissolution reactions increased the aqueous phase pH locally, leading to secondary $CaCO_3$ precipitation that reduced porosity (and permeability). The relationship between crystal saturation (S_c) and gas saturation (S_g) for the entire pore network, as depicted in the bottom images presented in Fig. 6 shows reduced S_c (up to 25%) in the inlet region that lowered the capillary pressure (changed pore morphology) and increased S_g. Secondary carbonate precipitation and CO_2 mineralization in the outlet regions lead to

the increase of S_c (45 h). After 67 h, crystals located near the inlet (port 1) and outlet (port 4) underwent either dissolution or detachment from the pore due to the injection of CO_2. The results were comparable to single pore observations (see Fig. 3): the injection of CO_2 caused the reduction of the aqueous phase pH and initiated carbonate crystal dissolution; the dissolution reaction in the inlet enlarged the pore throats and increased porosity locally; over time, secondary precipitation and CO_2 mineralization became the dominating geochemical reactions (predominantly in the outlet), leading to increasing S_c. The spatial distribution of crystal in the pore network highlights the dynamics of CO_2-water-mineral interactions in porous media, where the continuous flow of CO_2 could cause changes in the distribution of crystals, ultimately influencing the porosity, permeability, and fluid flow, particularly in near wellbore regions.
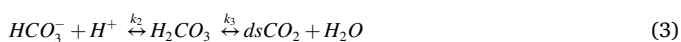
The comprehensive assessments above shed light on the compounded processes of CO_2-water–mineral interactions during CO_2 injection, and their coupling to multiphase flow in subsurface reservoirs in the context of carbon storage in carbonate-mineral rich formations. These geochemical reactions, including carbonate dissolution, secondary precipitation, CO_2 exsolution and mineralization can change the morphology, porosity, permeability, and wettability of the storage formation and influence storage efficiency, injectivity and safety.
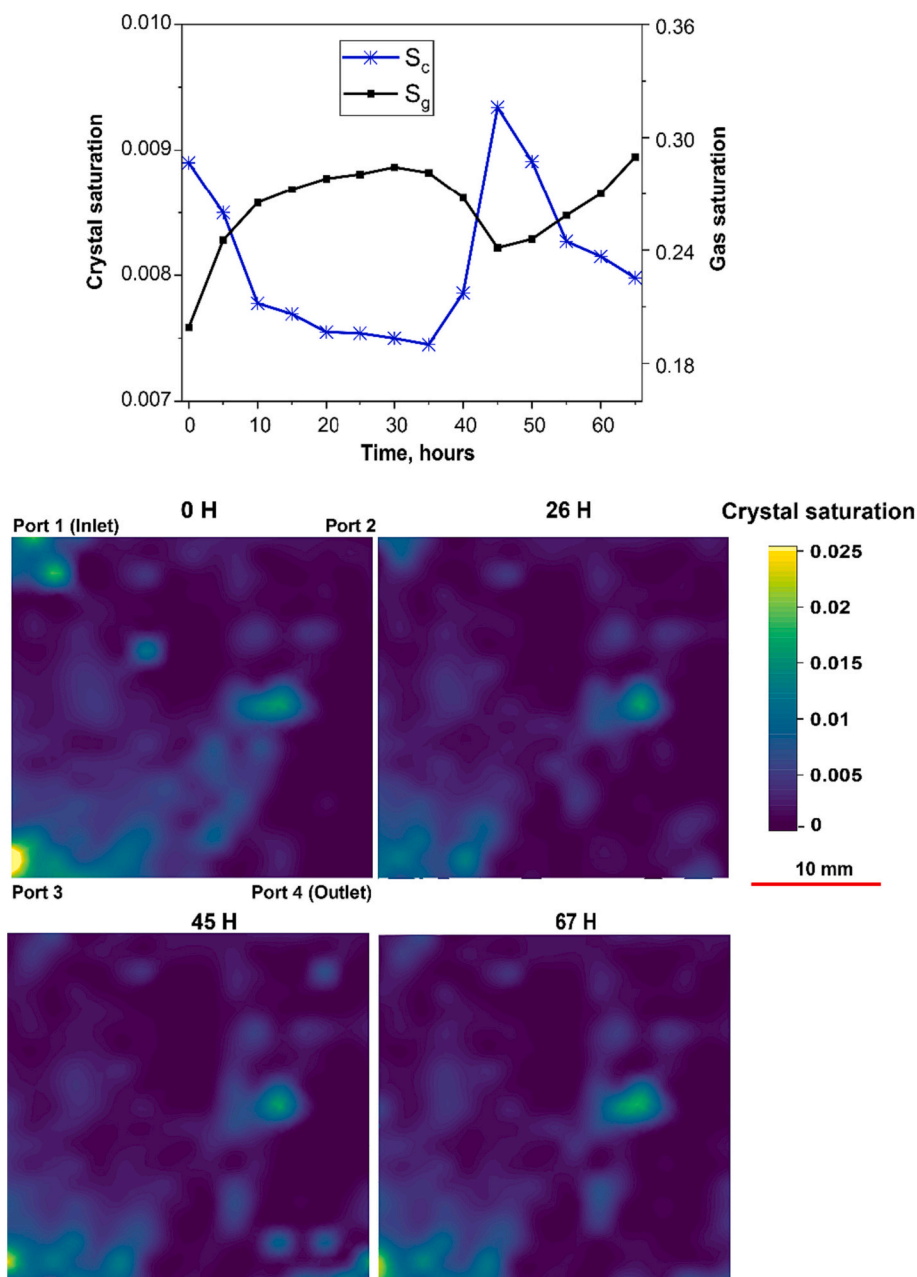
Fig. 6. Carbonate crystal saturation changes (entire pore network) during primary drainage scCO$_2$ injection (Exp M1). <u>Top row</u>: Crystal saturation (S_c) and gas saturation (S_g) as a function of time. <u>Bottom row</u>: Spatial distribution (contour plots) of local crystal saturation over time. <u>Note</u>: The pixel-based S_c was calculated under the assumption that each crystal pixel fills the entire pore space height (30 μm) and should be considered as an upper bound.

3.4. Kinetics of carbonate dissolution in the pore network

The CaCO$_3$ dissolution kinetics in porous media are primary dominated by surface-controlled chemical reactions and mass transfer resistance (Kaufmann and Dreybrodt, 2007; Liu and Dreybrod, 1997; Morse, 2018; Yoon et al., 2019). At the solid–fluid interface, the following parallel reactions (Plummer et al., 1978) occur:

$$CaCO_3 + H^+ \overset{k_1}{\rightarrow} Ca^{2+} + HCO_3^- \tag{2}$$

$$HCO_3^- + H^+ \overset{k_2}{\leftrightarrow} H_2CO_3 \overset{k_3}{\leftrightarrow} dsCO_2 + H_2O \tag{3}$$

where the rate coefficient k_i (i.e., k_{1-3}) is temperature dependent.

Carbonate dissolution (Reaction 2) is solely influenced by the concentration of H$^+$ ions (a_{H+}) in aqueous phase, and the aqueous phase pH equals to -log(a_{H+}). On the other hand, hydrolysis of H$_2$CO$_3$ (Reaction 3) depends on the CO$_2$ partial pressure and temperature (Kaufmann and Dreybrodt, 2007). As k_i remained constant in this study, the carbonate dissolution was primarily influenced by the aqueous phase and the CO$_2$ partial pressure. Determining parameters for the dissolution rate are directly linked to experimental operating conditions including aqueous phase pH, flow velocity, interface area, and pore geometry. These conditions allow for a systematic and controlled investigation of porous media dissolution kinetics (Fig. 7 **A**).

The average carbonate dissolution rate in the entire pore network decreased linearly with increasing pH, with a strong correlation between the rate of dissolution and a_{H+} (Fig. 7 **B**). This suggests that pH plays a significant role in controlling the (averaged) dissolution rate of the entire pore network, consistent with our claim that the chemical reaction at the solid-fluid interface (Reaction 2) is the primary mechanism
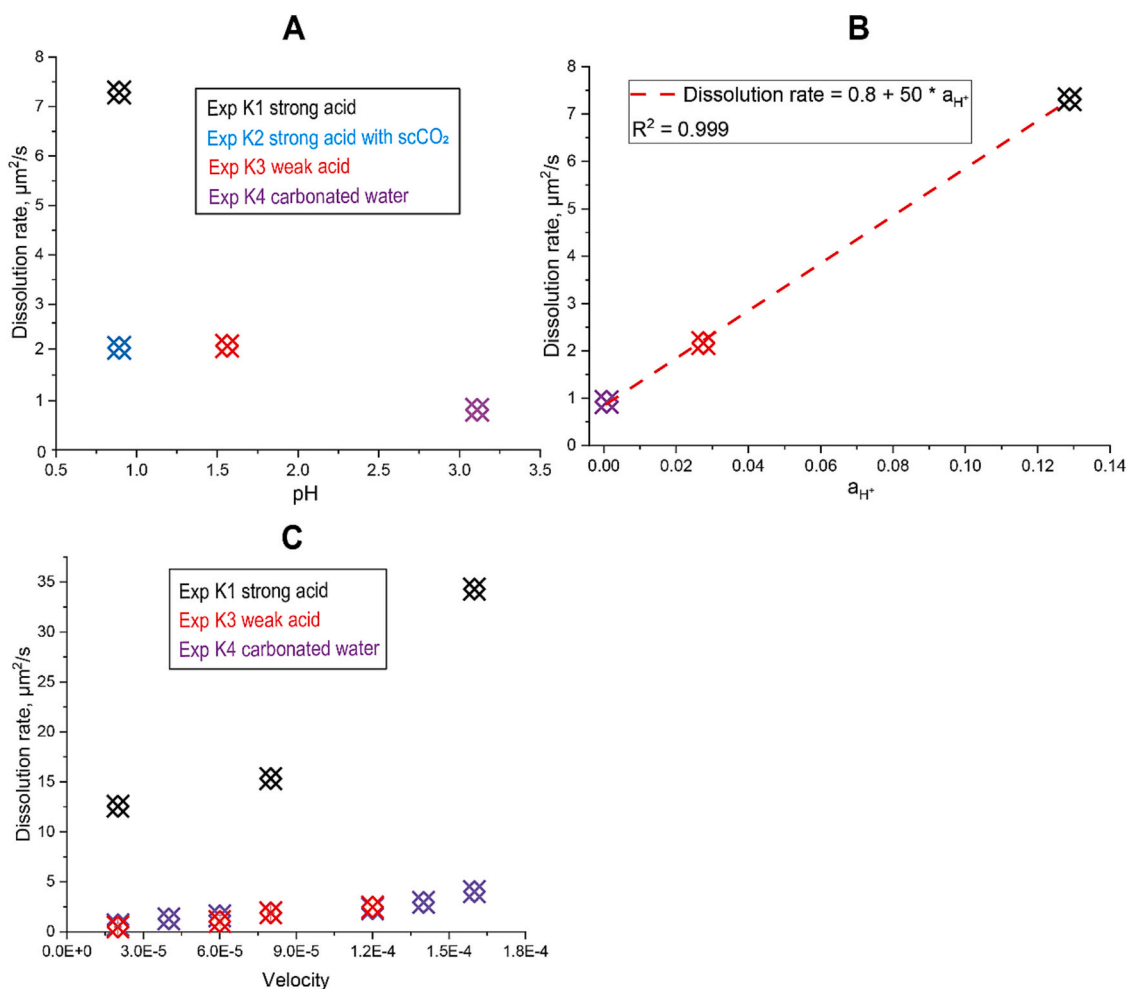
Fig. 7. Carbonate dissolution rate as a function of aqueous phase pH, H^+ concentration (a_{H+}) and local flow velocity. Detailed information regarding the experimental conditions is available in Table 2. Plot A: The dissolution rate is reduced with increasing aqueous phase pH, where the lowest pH (0.86, Exp K1) showed the highest dissolution rate (7.31 $\mu m^2/s$). The presence of a free $scCO_2$ phase (Exp K2) reduced the dissolution rate by 70% relative to the same pH (0.86, Exp K1), discussed more below. Plot B: The experimentally verified linear relationship between the dissolution rate and a_{H+} in porous media. Plot C: Dissolution rate as a function of local flow velocity increased linearly for three different aqueous phase pH values. Note that the flow velocity field was simulated without the presence of carbonate crystals (Landa-Marbán, 2023; Liu et al., 2023). The dissolution rate used was the average for the entire pore network for each experiment (K1-K4).

for carbonate dissolution in porous media. Locally in single pores, however, the miscible displacement of formation water (by the injected acid solutions) enabled transport of H^+ ions across the liquid-solid interface to contact the crystal surface. Hence, local hydrodynamics plays a crucial role for the mass transfer at the liquid-solid interface (Liu and Dreybrod, 1997). The local flow velocities strongly affect the shear stress and transfer of H^+ at the interface (Lv et al., 2021), resulting in locally varying dissolution rates in the pore network. We observed that the dissolution rate increased linearly with flow velocity for three different aqueous phase pH values (Fig. 7 C). Higher velocities induced higher shear stress and enhanced the mass transfer at the interface to accelerate the dissolution process. Hence, the mass transfer at the interface between the liquid and solid phases is essential for the local (single pore) dissolution process. Furthermore, the crystal surface was hydrophilic and coated with a water film (depicted in the upper-right images of Fig. 8), emphasizing the importance of mass transfer at the interface because hydrophilic surfaces may reduce the transport of H^+ ions to the crystal surface.

3.5. Effect of a free CO_2 phase on carbonate dissolution

The CO_2 phase (either injected or exsolved) determined the local dissolution rate by effectively blocking the diffusion of H^+ in the solid-liquid interface through a protective shield for engulfed crystals (Fig. 8). The exsolved CO_2 bubbles consistently nucleated at the surface of crystal, merged and engulfed the crystal to reduce the dissolution rate by almost 90%. The merging of CO_2 bubbles eventually led to partial detachment from the crystal surface, thereby allowing the dissolution process to resume at a higher rate. The dissolution rate reduction suggested that the presence of CO_2 bubbles also decreased the reactive surface area and the reaction rate (Song et al., 2018). Comparatively, the dissolution rate of crystals in the aqueous phase was initially much higher than that of crystals within the CO_2 phase, a distinction captured in the bottom images of Fig. 8. As depicted in the upper-right images of Fig. 8, the crystals exhibited hydrophilic properties and were covered with a water film (even when fully engulfed by a CO_2 phase). The water film facilitated the re-establishment of a chemical equilibrium between H^+, H_2CO_3 and $CaCO_3$ contributing to further inhibit dissolution. The presence of exsolved CO_2 led to an elevation in both the CO_2 partial pressure and the concentration of HCO_3^- within the solution. In addition, the a_{H^+} in the isolated water film on engulfed carbonate crystals decreased with reaction, leading to an increased aqueous phase pH surrounding the crystal and decreased dissolution rate.
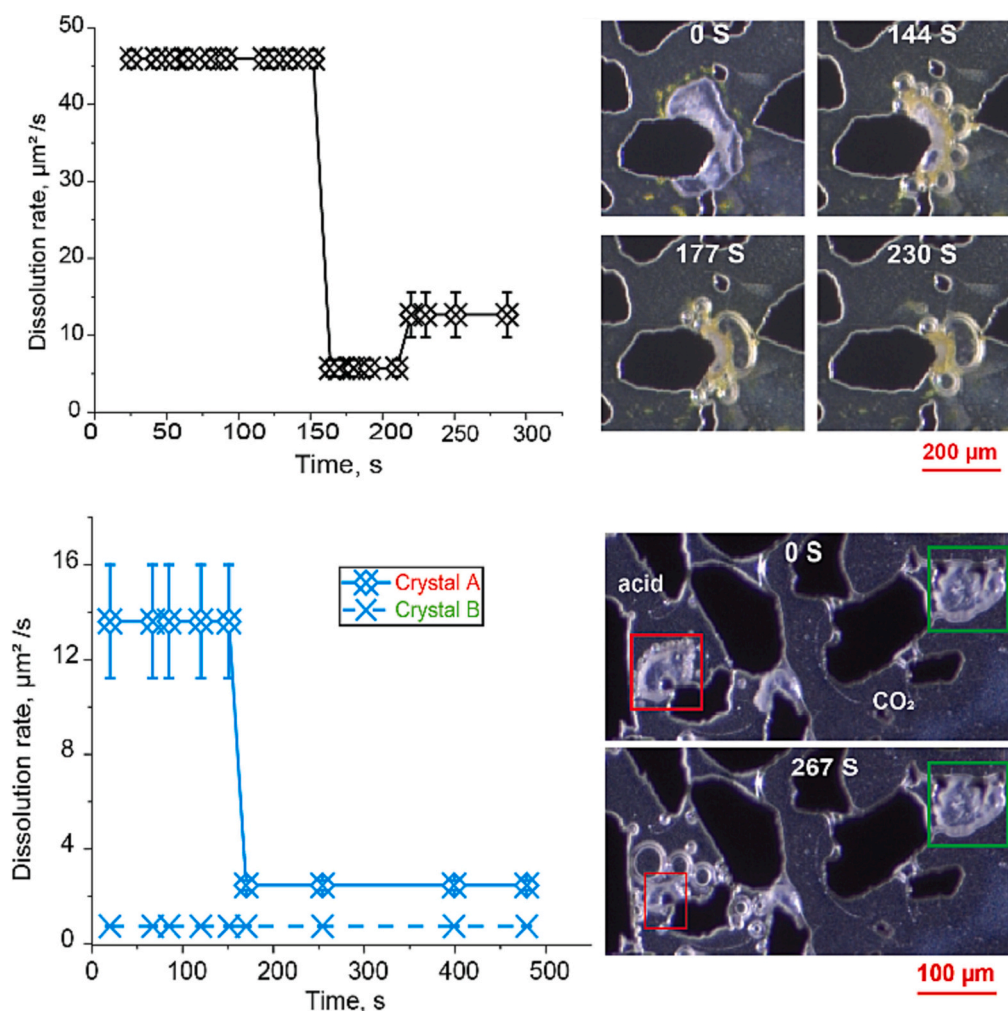
Fig. 8. Plots of crystal dissolution rate with and without the protection from CO_2 and time-series images of CO_2 exsolution from the crystal surface. <u>Top</u>: The high initial dissolution rate (45.95 $\mu m^2/s$) was reduced to 5.71 $\mu m^2/s$ due to CO_2 exsolution from the crystal surface in the presence of a 'strong' acid (Exp K1). <u>Bottom</u>: The dissolution rate of crystal A (red square) was initially 13.61 $\mu m^2/s$, almost 20 times higher than of crystal B (green square, 0.74 $\mu m^2/s$) (Exp K2). The dissolution rate for crystal A decreased when the crystal was engulfed by exsolved CO_2 bubbles. (For interpretation of the references to colour in this figure legend, the reader is referred to the web version of this article.)

### 3.6. Pore geometry affecting the dissolution pattern

Local crystal saturation (and hence, porosity) and reactive surface area changed during injection of carbonated water (Fig. 9). The produced reactant ions (i.e., HCO_3^- and Ca^{2+}) upstream increased the aqueous phase pH and shifted the chemical equilibrium for downstream dissolution reactions. With increasing local porosity (due to dissolved crystals), the injected aqueous phase bypassed the low-permeable regions with remaining $CaCO_3$ crystals. Surface reaction (Reaction 2), as opposite to mass transfer, controlled the dissolution process ($t \leq 200$ min) because a separate CO_2 phase (from exsolution or injection) was not present; corroborated with the linear decrease in crystal number (and porosity) in the pore network (**Fig. S1**). The process became mass transfer-controlled ($t > 200$ min), with decreased dissolution rate because the tortuous pore geometry induced mass transfer resistance.

The spatially dependent dissolution rate demonstrated the strong coupling between reactive surface area and hydrodynamics on the dissolution process (plots in Fig. 9). Initially, the inlet area dissolution rate was higher than that in middle and outlet area due to the low pH value. After 100 min, > 90% of inlet area crystals were dissolved, associated with increased local porosity and improved water injectivity. The larger outlet A_{rs} (2.4 times larger than the middle) resulted in a higher dissolution rate. After 200 min, most crystals in the inlet and

middle were dissolved, and the dissolution rate approached zero. The outlet dissolution was low (89% reduction from onset), but nonzero, due to residual crystals located in low-velocity zones. The upstream dissolution increased dissolved species and decreased the aqueous phase pH, resulting in reduction of the reaction rate in the middle and outlet areas relative to the inlet. A larger reactive surface area at the outlet promoted a higher dissolution rate. This observation aligns with previous findings (Yang et al., 2018; Yoon et al., 2012), highlighting that the dissolution rate scaled linearly with the available reactive surface area for Reaction 2. Crystals positioned in high-velocity zones dissolved first, whereas residual crystals predominantly accumulated in low-velocity zones near the outlet. These findings emphasize the influence of local flow velocity and available reactive surface area for $CaCO_3$ dissolution in the presence of carbonated water.

4. Conclusions

Our experimental pore-scale observations of carbonate dissolution kinetics show the interplay between CO_2 exsolution/mineralization and mineral dissolution/precipitation during CO_2 injection. These couped processes directly impact key GCS reservoir properties (e.g., porosity and permeability), and determine local transport and mobility of CO_2 in a storage formation. Furthermore, we observed that the $CaCO_3$
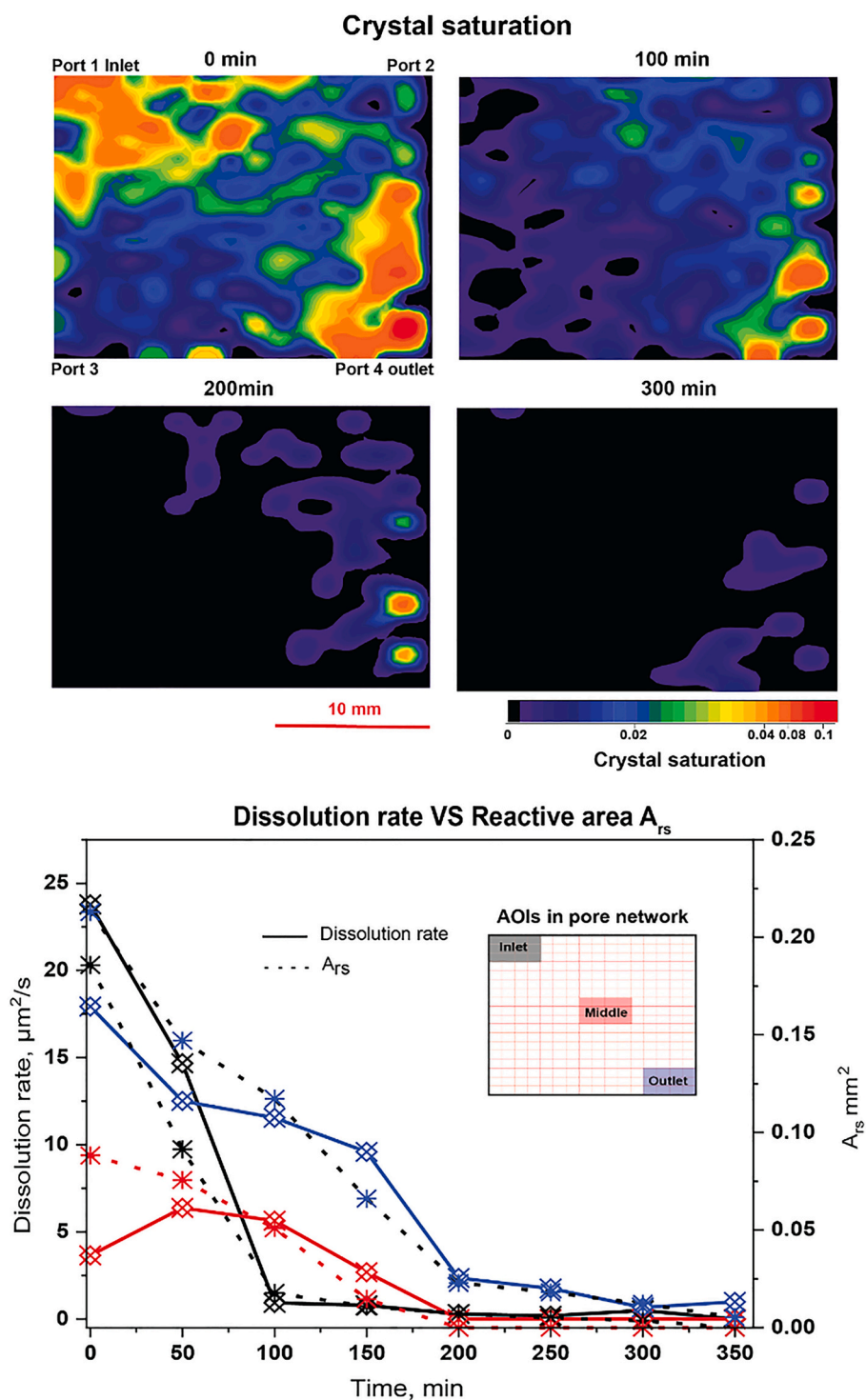
Fig. 9. Temporal changes of local crystal saturation (S_c), dissolution rate and reactive surface area (A_{rs}) during carbonated water injection (Exp K4). <u>Top:</u> The spatially distributed averaged unit S_c shown for four times: 0 min: at the onset, inlet and outlet regions have the highest crystal saturation; 100 min: the inlet S_c was reduced by 84% by dissolution, with an associated porosity increased by 3.7%. Outlet S_c, in comparison, was reduced by 50% where large crystals were only partly dissolved; 200 min: most of the crystals were dissolved, with some larger crystals remaining (right side); 300 min: only a few crystals located in narrow pores with low velocity and reduced mass transfer were observed. <u>Bottom:</u> Development in the average dissolution rate and reactive surface area (A_{rs}) for three areas of interest (see inset). <u>Note:</u> A_{rs} calculations use the perimeter of crystals multiplied by the depth of micromodel (30 μm). To illustrate the S_c changes more clearly, contour lines in plots were smoothed with a parameter of 9.84E-4, and spatially distributed crystal number and size in the pore network are presented in **Fig. S2**.

dissolution rate was significantly influenced by local chemical reactions and hydrodynamics. The dissolution rate increased with the reactive surface area and decreased with the pH of the aqueous phase, and the mass transfer in the diffusion boundary layer at the solid-liquid interface was controlled by local hydrodynamics. The presence of a free CO_2 phase (injected or exsolved) impedes the carbonate dissolution by reducing the reactive surface area and blocking the mass transport in the interface.

The MICP process as a mitigation technology for GCS leakage is susceptible to dissolution by CO_2-acidified brine, influencing its sealing

integrity near wellbores. The stability of MICP sealing may, however, improve over time if the carbonate crystals located in the low permeable area or the crystals become engulfed by CO_2 gas that inhibit dissolution. Hence, we argue that the coupled dissolution/precipitation processes, including the CO_2 exsolution process (releasing a mobile and buoyant CO_2 phase), needs to be considered when evaluating GCS leakage risk scenarios.

Our analysis focuses on hydrophilic carbonate crystals via the uratolytic pathway (using *Sporosarcina pasteurii* stains), resulting in a high dissolution rate due to the water film. To gain a more comprehensive understanding, further investigation is necessary to examine the influence of surface properties of crystals on the dissolution rate.

Declaration of Competing Interest

The authors declare that they have no known competing financial interests or personal relationships that could have appeared to influence the work reported in this paper.

Data availability

Data will be made available on request.

Acknowledgements

Appendix A. Supplementary data

Supplementary data to this article can be found online at https://doi.org/10.1016/j.chemgeo.2023.121782.

References

Al-Amshawee, S., et al., 2021. Roughness and wettability of biofilm carriers: a systematic review. Environ. Technol. Innov. 21, 101233.

Allison, C.M., Roggensack, K., Clarke, A.B., 2021. Highly explosive basaltic eruptions driven by CO_2 exsolution. Nat. Commun. 12 (1), 217.

Bachu, S., Gunter, W., Perkins, E., 1994. Aquifer disposal of CO_2: hydrodynamic and mineral trapping. Energy Convers. Manag. 35 (4), 269–279.

Benali, B., et al., 2022. Pore-scale bubble population dynamics of CO_2-foam at reservoir pressure. Int. J. Greenhouse Gas Control 114.

Buhmann, D., Dreybrodt, W., 1985. The kinetics of calcite dissolution and precipitation in geologically relevant situations of karst areas: 1. Open system. Chem. Geol. 48 (1–4), 189–211.

Cao, S., Jung, J., Hu, J., 2015. CO2-brine displacement in geological CO2 sequestration: microfluidic flow model study. Appl. Mech. Mater. 752-753, 1210–1213.

Chang, C., et al., 2016. Pore-scale supercritical CO_2 dissolution and mass transfer under imbibition conditions. Adv. Water Resour. 92, 142–158.

Chang, C., Zhou, Q., Oostrom, M., Kneafsey, T.J., Mehta, H., 2017. Pore-scale supercritical CO_2 dissolution and mass transfer under drainage conditions. Adv. Water Resour. 100, 14–25.

Coto, B., Martos, C., Peña, J.L., Rodríguez, R., Pastor, G., 2012. Effects in the solubility of CaCO3: Experimental study and model description. Fluid Phase Equilib. 324, 1–7.

Cunningham, A.B., et al., 2011. Reducing the risk of well bore leakage of CO2 using engineered biomineralization barriers. Energy Procedia 4, 5178–5185.

Cunningham, A.B., et al., 2014. Wellbore leakage mitigation using engineered biomineralization. Energy Procedia 63, 4612–4619.

Deng, H., et al., 2013. Modifications of carbonate fracture hydrodynamic properties by CO2-acidified brine flow. Energy Fuel 27 (8), 4221–4231.

Deng, H., Fitts, J.P., Crandall, D., McIntyre, D., Peters, C.A., 2015. Alterations of fractures in carbonate rocks by CO2-acidified brines. Environ. Sci. Technol. 49 (16), 10226–10234.

Dhar, J., Meunier, P., Nadal, F., Méheust, Y., 2022. Convective dissolution of carbon dioxide in two- and three-dimensional porous media: the impact of hydrodynamic dispersion. Phys. Fluids 34 (6), 064114.

Duan, Z., Sun, R., 2003. An improved model calculating CO2 solubility in pure water and aqueous NaCl solutions from 273 to 533 K and from 0 to 2000 bar. Chem. Geol. 193 (3), 257–271.

Ellis, B.R., Crandell, L.E., Peters, C.A., 2010. Limitations for brine acidification due to SO2 co-injection in geologic carbon sequestration. Int. J. Greenhouse Gas Control 4 (3), 575–582.

Gadikota, G., 2021. Carbon mineralization pathways for carbon capture, storage and utilization. Communicat. Chem. 4 (1), 23.

Grogan, A., Pinczewski, V., Ruskauff, G.J., Orr, F., 1988. Diffusion of CO2 at reservoir conditions: models and measurements. SPE Reserv. Eng. 3 (01), 93–102.

Haugen, M., et al., 2023a. Calcite-functionalized micromodels for pore-scale investigations of CO 2 storage security. E3S Web Conf. 366, 01004.

Haugen, M., Brattekås, B., Fernø, M., 2023b. Multimodal Visualization of Calcium Carbonate (CaCO3) in the Pore Space of a Micromodel. In: Médici, E.F., Otero, A.D. (Eds.), Album of Porous Media: Structure and Dynamics. Springer International Publishing, Cham, p. 95.

Hellevang, H., Wolff-Boenisch, D., Nooraiepour, M., 2019. Kinetic Control on the Distribution of Secondary Precipitates during CO2-Basalt Interactions, E3S Web of Conferences.

Kaufmann, G., Dreybrodt, W., 2007. Calcite dissolution kinetics in the system CaCO3–H2O–CO2 at high undersaturation. Geochim. Cosmochim. Acta 71 (6), 1398–1410.

Kazemifar, F., Blois, G., Kyritsis, D.C., Christensen, K.T., 2016. Quantifying the flow dynamics of supercritical CO2–water displacement in a 2D porous micromodel using fluorescent microscopy and microscopic PIV. Adv. Water Resour. 95, 352–368.

Kordač, M., Linek, V., 2008. Dynamic measurement of carbon dioxide volumetric mass transfer coefficient in a well-mixed reactor using a pH Probe: analysis of the salt and supersaturation effects. Ind. Eng. Chem. Res. 47 (4), 1310–1317.

Landa-Marbán, D., 2023. daavid00/pymm: Release 2023.10 (v2023.10).

Le Chatelier, H.L., 1884. A general statement of the laws of chemical equilibrium. Comptes Rendus 99, 786–789.

Liu, Z., Dreybrod, W., 1997. Dissolution kinetics of calcium carbonate minerals in H2O-CO2 solutions in turbulent flow: the role of the diffusion boundary layer and the slow reaction H2O + CO2 → H+ + HCO3−. Geochim. Cosmochim. Acta 61 (14), 2879–2889.

Liu, N., Haugen, M., Benali, B., Landa-Marbán, D., Fernø, M.A., 2023. Pore-scale spatiotemporal dynamics of microbial-induced calcium carbonate growth and distribution in porous media. Int. J. Greenhouse Gas Control 125, 103885.

Lu, P., et al., 2013. Coupled alkali feldspar dissolution and secondary mineral precipitation in batch systems – 2: New experiments with supercritical CO2 and implications for carbon sequestration. Appl. Geochem. 30, 75–90.

Lv, H., et al., 2021. Liquid flow and mass transfer behaviors in a butterfly-shaped microreactor. Micromachines (Basel) 12 (8).

Miri, R., Hellevang, H., 2016. Salt precipitation during CO2 storage—a review. Int. J. Greenhouse Gas Control 51, 136–147.

Mitchell, A.C., et al., 2013. Microbial CaCO3 mineral formation and stability in an experimentally simulated high pressure saline aquifer with supercritical CO2. Int. J. Greenhouse Gas Control 15, 86–96.

Molins, S., et al., 2014. Pore-scale controls on calcite dissolution rates from flow-through laboratory and numerical experiments. Environ. Sci. Technol. 48 (13), 7453–7460.

Morais, S., et al., 2016. Monitoring CO2 invasion processes at the pore scale using geological labs on chip. Lab Chip 16 (18), 3493–3502.

Morse, J.W., 2018. Chapter 7. the kinetics of calcium carbonate dissolution and precipitation. In: Richard, J.R. (Ed.), Carbonates: Mineralogy and Chemistry. De Gruyter, pp. 227–264.

Morse, J.W., Arvidson, R.S., Lüttge, A., 2007. Calcium carbonate formation and dissolution. Chem. Rev. 107 (2), 342–381.

Oelkers, E.H., Gislason, S.R., Matter, J., 2008. Mineral carbonation of CO2. Elements 4 (5), 333–337.

Pachauri, R.K., Reisinger, A., 2007. IPCC Fourth Assessment Report. IPCC, Geneva, p. 2007.

Phillips, A.J., et al., 2013. Potential CO2 Leakage Reduction through Biofilm-Induced Calcium Carbonate Precipitation. Environ. Sci. Technol. 47 (1), 142–149.

Plummer, L., TML, W., DL, P., 1978. The Kinetics of Calcite Dissolution in CO2-Water Systems at 5O to 60OC and 0.0 to 1.0 ATM CO2.

Rezk, M.G., Foroozesh, J., Abdulrahman, A., Gholinezhad, J., 2022. CO2 diffusion and dispersion in porous media: review of advances in experimental measurements and mathematical models. Energy Fuel 36 (1), 133–155.

Scientific, T., 2022. pHrodoTM Red, Succinimidyl Ester (pHrodoTM Red, SE).

Song, W., Ogunbanwo, F., Steinsbø, M., Fernø, M.A., Kovscek, A.R., 2018. Mechanisms of multiphase reactive flow using biogenically calcite-functionalized micromodels. Lab Chip 18 (24), 3881–3891.

Van der Walt, S., et al., 2014. Scikit-image: image processing in Python. PeerJ 2, e453.

Xu, J., Balhoff, M., 2022. Dissolution-After-Precipitation (DAP): a simple microfluidic approach for studying carbonate rock dissolution and multiphase reactive transport mechanisms. Lab Chip 22.

Xu, R., Li, R., Ma, J., He, D., Jiang, P., 2017. Effect of mineral dissolution/precipitation and CO2 exsolution on CO2 transport in geological carbon storage. Acc. Chem. Res. 50 (9), 2056–2066.

Yang, Y., et al., 2018. Retraction of the dissolution front in natural porous media. Sci. Rep. 8 (1), 5693.

Yoon, H., Valocchi, A.J., Werth, C.J., Dewers, T., 2012. Pore-scale simulation of mixing-induced calcium carbonate precipitation and dissolution in a microfluidic pore network. Water Resour. Res. 48 (2).

Yoon, H., Chojnicki, K.N., Martinez, M.J., 2019. Pore-scale analysis of calcium carbonate precipitation and dissolution kinetics in a microfluidic device. Environ. Sci. Technol. 53 (24), 14233–14242.

Zhang, C., Oostrom, M., Grate, J.W., Wietsma, T.W., Warner, M.G., 2011. Liquid CO2 displacement of water in a dual-permeability pore network micromodel. Environ. Sci. Technol. 45 (17), 7581–7588.

Zhu, C., Lu, P., 2009. Alkali feldspar dissolution and secondary mineral precipitation in batch systems: 3. Saturation states of product minerals and reaction paths. Geochim. Cosmochim. Acta 73 (11), 3171–3200.